nature materials

Article

https://doi.org/10.1038/s41563-023-01612-2

Li iontronics in single-crystalline T-Nb_2O_5 thin films with vertical ionic transport channels

Received: 13 April 2022

Accepted: 19 June 2023

Published online: 27 July 2023

Check for updates

Hyeon Han[1,8] ✉, Quentin Jacquet[2,7,8], Zhen Jiang[3,8], Farheen N. Sayed[2], Jae-Chun Jeon[1], Arpit Sharma[1], Aaron M. Schankler[3], Arvin Kakekhani[3], Holger L. Meyerheim[1], Jucheol Park[4], Sang Yeol Nam[4], Kent J. Griffith[5], Laura Simonelli[6], Andrew M. Rappe[3] ✉, Clare P. Grey[2] ✉ & Stuart S. P. Parkin[1] ✉

The niobium oxide polymorph T-Nb_2O_5 has been extensively investigated in its bulk form especially for applications in fast-charging batteries and electrochemical (pseudo)capacitors. Its crystal structure, which has two-dimensional (2D) layers with very low steric hindrance, allows for fast Li-ion migration. However, since its discovery in 1941, the growth of single-crystalline thin films and its electronic applications have not yet been realized, probably due to its large orthorhombic unit cell along with the existence of many polymorphs. Here we demonstrate the epitaxial growth of single-crystalline T-Nb_2O_5 thin films, critically with the ionic transport channels oriented perpendicular to the film's surface. These vertical 2D channels enable fast Li-ion migration, which we show gives rise to a colossal insulator–metal transition, where the resistivity drops by 11 orders of magnitude due to the population of the initially empty Nb $4d^0$ states by electrons. Moreover, we reveal multiple unexplored phase transitions with distinct crystal and electronic structures over a wide range of Li-ion concentrations by comprehensive in situ experiments and theoretical calculations, which allow for the reversible and repeatable manipulation of these phases and their distinct electronic properties. This work paves the way for the exploration of novel thin films with ionic channels and their potential applications.

The control of the electronic properties of materials via voltage biasing forms the cornerstone of many electronic applications. A recent trend in the field has been to leverage ionic liquid gating (ILG) of oxides, enabling the electric-field control of insulator-to-metal transitions. These electronic transitions via ILG are typically induced by the electrochemical intercalation of O^{2-} or H^+ ions[1–13], which can, however, be sluggish, poorly controlled or involve degradation of the electrolyte[6]. Alternatively, intercalation of Li^+ ions into oxides can provide fast ion

[1]Max Planck Institute of Microstructure Physics, Halle (Saale), Germany. [2]Yusuf Hamied Department of Chemistry, University of Cambridge, Cambridge, UK. [3]Department of Chemistry, University of Pennsylvania, Philadelphia, PA, USA. [4]Test Analysis Research Center, Gumi Electronics and Information Technology Research Institute, Gumi, Republic of Korea. [5]Department of Chemistry, Northwestern University, Evanston, IL, USA. [6]ALBA Synchrotron Light Source, Cerdanyola del Vallès, Barcelona, Spain. [7]Present address: Univ. Grenoble Alpes, CEA, CNRS, IRIG, SyMMES, Grenoble, France. [8]These authors contributed equally: Hyeon Han, Quentin Jacquet, Zhen Jiang. ✉e-mail: hyeonhan21@gmail.com; rappe@sas.upenn.edu; cpg27@cam.ac.uk; stuart.parkin@mpi-halle.mpg.de

https://doi.org/10.1038/s41563-023-01612-2

diffusion, and, thereby, is fundamental to diverse applications, ranging from Li-ion batteries[14–19] and electrochromics[20–22] to electronic devices[23–30]. WO_3 is known as one of the best-performing electrochemical materials for Li-ionic gating, owing to the large resistance change (up to approximately seven orders of magnitude), fast response and good endurance[9,10,29]. However, this material and its thin-film form can show a limited voltage operation range due to the conversion reaction that occurs with Li ions[31]. Thus, finding new thin-film systems that exhibit rapid and large changes in properties with high stability via Li-ion intercalation can boost various applications. Moreover, understanding the correlation between structure, electrochemical and electronic properties during Li-ion insertion is needed to realize repeatable manipulation of these properties.

T-Nb_2O_5 is a promising material, which is known as an anode material for applications in batteries and electrochemical capacitors/pseudocapacitors[32–38]. Fast Li-ion diffusion in *T*-Nb_2O_5 is enabled by its crystal structure, consisting of two-dimensional (2D) layers at 4*g* Wyckoff positions of the space group *Pbam*, with very low steric hindrance for intralayer Li-ion diffusion[37,39] (Fig. 1a and Supplementary Fig. 1). Moreover, *T*-Nb_2O_5 is a d^0 insulator, and Li-ion intercalation is expected to increase the electronic conductivity by filling the Nb 4*d* levels (Fig. 1b, left inset), making *T*-Nb_2O_5 a promising candidate for switchable electronic applications. However, since the discovery of *T*-Nb_2O_5 in 1941[37], the single-crystalline thin-film growth and its electronic properties have not been demonstrated. This difficulty is probably due to its large orthorhombic unit cell (a = 6.175 Å, b = 29.175 Å, c = 3.930 Å)[39], its metastability[32] and the presence of many other Nb_2O_5 polymorphs that are close in energy[38].

Here, we demonstrate epitaxial growth of high-quality single-crystalline *T*-Nb_2O_5 thin films oriented with their (180) plane parallel to the surface such that 2D open channels in the crystal structure are ideally oriented perpendicular to the film surface. Li-containing ionic liquid gating (Li-ILG) of *T*-Nb_2O_5 thin films results in a fast and colossal insulator–metal transition with approximately 11 orders of magnitude increase in the resistivity of the material during the early stages of Li insertion. Multiple unexplored phase transitions, including an orthorhombic metal and a monoclinic metal, are found in thin-film forms, while the bulk material further reveals a tetragonal phase at high Li concentrations. These new phases were observed by comprehensive in situ experiments and rationalized with the help of density functional theory (DFT) calculations. This understanding enables repeatable and durable control of electronic properties by operating within the reversible phase transition range of the crystalline thin films. Furthermore, a tunable metallization voltage is demonstrated by altering the chemical potential of the gate electrode via the use of lithiated counter electrodes.

Growth of epitaxial thin films having vertical ionic channels

Pulsed laser deposition (PLD) was used to grow *T*-Nb_2O_5 thin films on (001)- and (110)-oriented substrates of $LaAlO_3$ (LAO) and $(La_{0.18}Sr_{0.82})(Al_{0.59}Ta_{0.41})O_3$ (LSAT). Various polymorphs, including the TT-, T-, B- and H-Nb_2O_5 phases, were identified by X-ray diffraction that strongly depend on the growth temperature (Supplementary Fig. 2a). Single-phase *T*-Nb_2O_5(180) films were obtained for growth temperatures between 600 and 650 °C. Cross-sectional scanning transmission electron microscopy (STEM) was used to obtain high-angle annular dark-field (HAADF) images and Fourier transformation patterns (Fig. 1b and Supplementary Fig. 3). When using conventional (001)-oriented substrates, multidomains with the four-fold symmetry, rotated in-plane by 90° with respect to each other, were formed, as previously observed for growth on $SrTiO_3$ (001)[40]. However, the growth of two-fold symmetric *T*-Nb_2O_5(180) thin films was realized by using (110)-oriented substrates. Reflection high-energy electron diffraction (RHEED) patterns and X-ray diffraction phi-scans further confirmed this

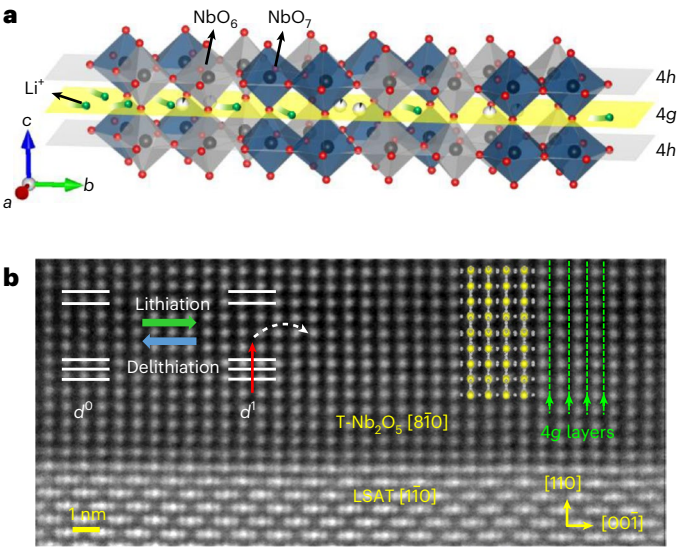

Fig. 1 | Structure of epitaxial *T*-Nb_2O_5 thin films. a, Schematic showing Li-ion migration into *T*-Nb_2O_5. The black, red and green spheres denote Nb, O and Li ions, respectively. The grey and navy polyhedra denote distorted octahedra (NbO_6) and pentagonal bipyramids (NbO_7), respectively. The grey and yellow planes represent the 4*h* and 4*g* layers, respectively. The loosely packed 2D 4*g* layer provides for fast Li-ion transport. **b**, Cross-sectional HAADF-STEM image of a single-crystalline *T*-Nb_2O_5 thin-film grown on a LSAT(110) substrate viewed along the LSAT [1$\bar{1}$0] direction. Left inset, Nb 4*d* orbital state changes from d^0 to d^1 due to electron doping via Li intercalation. Overlaid yellow and grey spheres represent Nb and O atoms, respectively. Green dashed lines represent the vertical ionic transport channels (4*g* layers) viewed from *T*-Nb_2O_5 [8$\bar{1}$0].

finding (Supplementary Section 1). The anisotropic in-plane geometry of the (110)-oriented substrates probably prohibits the formation of multidomains[41]. Both thin films exhibit vertically oriented two-dimensional 4*g* layers (the green dashed lines in Fig. 1b and Supplementary Fig. 3) that are ideal for Li-ion transport.

Structural and electronic phase diagram by Li insertion

The evolution of the crystal structure correlated with corresponding changes of the electronic properties in *T*-Nb_2O_5 via Li-ion intercalation was investigated by various in situ and ex situ methods. X-ray diffraction patterns and resistance were measured during Li-ILG of a single-crystalline *T*-Nb_2O_5/LSAT(110) thin-film device using Au/Ru as the gate electrode (Fig. 2a and Supplementary Fig. 7). Between a gate voltage (V_g) of 0 and 3 V, there is no noticeable change in the (180) reflection position, while the resistance starts to decrease at $V_g \approx 2$ V, suggesting the onset of an insulator-to-metal transition without a notable structural modification. Beginning with V_g = 3.5 to 4 V, the (180) diffraction peak starts to shift towards lower angles without any change in resistance; this shift was assigned to a transition from orthorhombic to monoclinic phase by using reciprocal space maps (Supplementary Fig. 8). As shown in Supplementary Fig. 9, in the range V_g = 4 to −1 V, the (180) peak and resistance return to their original values, indicating the reversibility of the structural and electronic changes. At V_g = 6 V, concomitantly with the irreversible increase of resistance suggesting a metal-to-insulator transition, an amorphization of the film was observed, evidenced by a decrease of the (180) peak intensity together with TEM images (Supplementary Fig. 10), indicating a degradation of the thin film at high Li concentration.

In situ X-ray diffraction experiments were performed on polycrystalline *T*-Nb_2O_5 powder in a typical battery configuration[42] (Fig. 2b–f and Supplementary Section 2). During Li-ion insertion, a first structural phase transition is revealed at x = 0.8 in $Li_xNb_2O_5$ with a large shift in

https://doi.org/10.1038/s41563-023-01612-2

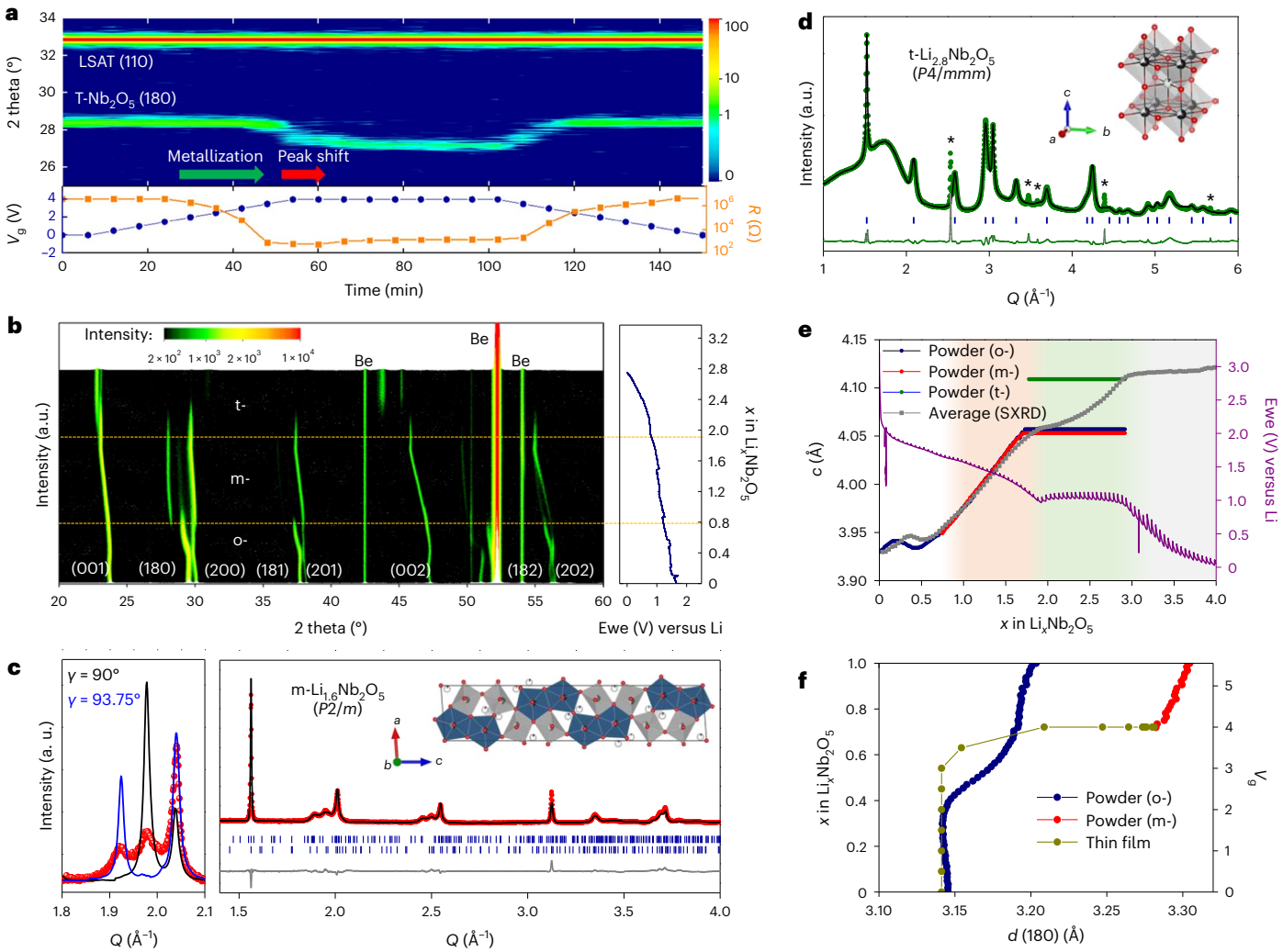

Fig. 2 | Sequential structural phase transitions of *T*-Nb_2O_5 via Li-ion intercalation. a, In situ X-ray diffraction and resistance measurements during Li-ILG of a 50 nm *T*-Nb_2O_5/LSAT(110). **b**, In situ X-ray diffraction patterns for powder *T*-Nb_2O_5 until the deep discharge potential of 0.005 V versus Li in 34 hours. 'Be' indicates peaks from the Be window. Horizontal yellow dashed lines indicate the boundary of the transitions. Ewe represents the working electrode potential. **c**, Ex situ SXRD pattern (red) of $Li_{1.6}Nb_2O_5$ and simulated patterns of the *Pbam* (black) and *P*2/*m* (blue) structural models. The (180) reflection is split by monoclinic tilting (left panel). SXRD pattern and Rietveld refinements of m-$Li_{1.6}Nb_2O_5$. Red circles, black line and grey line represent the observed, calculated and difference patterns, respectively. The black spheres, red spheres, grey polyhedra and navy polyhedra in the unit cell represent Nb ions, O ions, octahedra (NbO_6) and pentagonal bipyramids (NbO_7), respectively (right panel). **d**, Rietveld refinement of an in situ SXRD pattern measured at 5 mV using the t-phase. The in situ cell produces peaks marked as *. Green circles, black line and grey line represent the observed, calculated and difference patterns, respectively. Blue vertical bars represent the Bragg position. The black spheres, red spheres and grey polyhedra in the unit cell denote Nb ions, O ions and octahedra (NbO_6), respectively. Li positions are not considered in all refined structures due to the low scattering amplitude of Li ions. **e**, *c* lattice parameter as a function of *x* in $Li_xNb_2O_5$. Grey dots represent the average *c* parameter obtained from the SXRD data. Blue, red and green dots denote the *c* parameter of the o-, m- and t-phases, respectively, extracted from the in situ X-ray diffraction data. The purple line is the voltage curve obtained for a powder electrode in a coin cell during a galvanostatic measurement including open circuit voltage steps. Colour zones highlight four regions: (1) pristine *o*-phase from $Li_0Nb_2O_5$ to $Li_{0.8}Nb_2O_5$ (white), (2) a 25/75% mixture of the o- and m-phases from $Li_{0.8}Nb_2O_5$ to $Li_{1.8}Nb_2O_5$ (pink), (3) progressive formation of the t-phase from $Li_{1.8}Nb_2O_5$ to $Li_3Nb_2O_5$ (green), (4) no change of the X-ray diffraction pattern from $Li_3Nb_2O_5$ to $Li_4Nb_2O_5$ (grey). **f**, Comparison of the *d*(180) spacing for the powder and thin-film X-ray diffraction.

the (180) peak position along with the disappearance of the (181) peak (Fig. 2b and Supplementary Fig. 11). In addition, at a higher Li-ion content, $x \approx 1.8$, a second structural transition is observed. To unambiguously identify these unexplored structures, we performed synchrotron-based X-ray diffraction (SXRD) for the $Li_{0.8}Nb_2O_5$ and $Li_3Nb_2O_5$ phases. Rietveld refinement of ex situ SXRD pattern of $Li_{0.8}Nb_2O_5$ shows that the transition corresponds to a monoclinic (m-) distortion ($\gamma \approx 94°$) of the initial orthorhombic (o-) *T*-Nb_2O_5 structure without a notable change in the Nb framework (Fig. 2c, Supplementary Fig. 12 and Supplementary Table 1). Interestingly, ~25% of the crystal volume remains in the orthorhombic phase, while both phases are active for Li intercalation (Supplementary Fig. 15). This suggests that the driving force for the transition to the monoclinic phase of the powder is weak and, hence, in competition with other effects preventing the transition, such as strain or compositional heterogeneities. The second structural transition of the powder involves the formation of a new tetragonal (*t*-) Li-rich layered rock-salt structure with an approximate composition of $Li_3Nb_2O_5$ (Fig. 2d, Supplementary Fig. 13 and Supplementary Table 2). A recent report mentions the formation of a cubic phase, which can be viewed as a parent phase of this newly discovered tetragonal rock-salt phase, but which is characterized by a disordered Li/Nb site occupancy. Formed by lithiation of an amorphous Nb_2O_5

powder, it possesses excellent capacity at higher current densities and with a conductivity that is larger by approximately four orders of magnitude compared to the pristine phase[43]; but we note that this phase still belongs to the insulating regime and is in an irreversible transition range for the initially crystalline thin-film form. Having resolved all phases in the $Li_xNb_2O_5$, we report the evolution of the cell parameters as a function of Li-ion content together with the voltage (Fig. 2e).

The correlation between the in situ powder X-ray diffraction/SXRD and in situ thin-film X-ray diffraction measurements allows us to study the structural evolution as a function of Li concentration and V_g (Fig. 2f). The single-crystalline thin-film morphology enables monitoring of the change in electrical resistance as a function of Li-ion concentration and carrier mobility via Hall effect measurements (described later in Fig. 4h). These measurements therefore allow the correlation of the film's electronic properties with its structure. Finally, the Li-ion concentration-dependent electronic and structural phase diagram of the T-Nb_2O_5 thin film is obtained (Fig. 3a), revealing multistep phase transitions between the initial orthorhombic insulator ($x < 0.3$), an orthorhombic metal ($0.3 \leq x < 0.8$), a monoclinic metal ($0.8 \leq x < 1.8$) and an irreversible transition to an amorphous insulator ($x \geq 1.8$). The tetragonal phase observed by in situ SXRD of the powder sample was not observed in thin films, possibly because of a clamping effect via the substrate, which hinders this phase change and thus drives the amorphization. In particular, the early lithiation stage in T-Nb_2O_5 is promising for fast and reversible electronic applications due to the sharp conductivity change without the substantial structural change.

DFT calculations on T-Nb_2O_5 via lithiation

We investigated the evolution of the structural and electronic properties of T-Nb_2O_5 during lithiation through ab initio study. Here, we designed a new structural simulation model (Fig. 3b) for pristine T-Nb_2O_5 ($Nb_{16.8}O_{42}$) by eliminating the fractional occupancy of Nb and the resulting charge imbalance (Supplementary Section 3.2), resulting in a DFT-derived band gap of ~2.3 eV (Fig. 3c). Next, we studied the energetics and kinetics of Li interstitials in our model unit cell of [T-Nb_2O_5]. We found that Li interstitials are located within the 4g layer atop two-coordinated oxygen atoms with a marginally stronger binding energy ($\Delta E_b = -2.06$ eV, defined in Methods) than that of other sites (Supplementary Section 3.3). Then, we investigated Li diffusion along the minimum energy path from this site to sites atop neighbouring O atoms (Fig. 3g) and found an activation barrier of $E_a = 0.26$ eV. Since the diffusion barriers and energy differences for Li at different sites are both small, there is a high probability that the incorporated Li ions are not trapped in fixed locations.

To avoid spurious interactions between periodic images along the c direction, which has a small lattice periodicity, we model low Li concentrations by using supercells. With one extra Li inserted into an ($a \times b \times 3c$) supercell, the band gap is found to be greatly reduced (Fig. 3d) from 2.3 eV (in [T-Nb_2O_5]) to 0.3 eV (in $Li_{x=0.02}$-[T-Nb_2O_5] (x = Li/Nb)), because a new, filled defect band just below the Fermi energy (E_F) is induced by this Li interstitial (Supplementary Fig. 17b). After that, the material becomes metallic once a second extra Li is intercalated into the ($a \times b \times 3c$) supercell, as shown in Fig. 3e. This is because the newly induced band crosses the E_F (Supplementary Fig. 17c). In addition, we note that the size of the simulation supercell (especially that of the c axis) affects the Li concentration required to induce metallization (Supplementary Section 3.4). Therefore, ab initio calculations can provide a qualitative explanation for the rapid onset of metallization at low Li concentration.

Finally, we investigated the differential binding energy (ΔE_b) as a function of Li interstitial concentration in our [T-Nb_2O_5] model. For low Li concentrations (x = Li/Nb < 0.2), the obtained ΔE_b fluctuates around −2 eV (−1.95 eV to −2.24 eV) (Fig. 3h). With increasing Li concentration, the magnitude of ΔE_b gradually decreases, but it remains smaller than −1.5 eV until at least Li/Nb = 0.5. Moreover, we found that at higher Li concentration (Li/Nb ≈ 0.5) a phase transformation from orthorhombic to monoclinic is energetically favourable. Figure 3i shows the relative change of the total energy of the $Li_{x=0.54}$-[T-Nb_2O_5] structure as a function of the monoclinic tilt angle varying between 90° and 92.5°. The monoclinic phase with a tilt angle of about 91.4° is more stable than the orthorhombic one by 0.44 meV per atom, and it is consistent for other metastable configurations of $Li_{x=0.54}$-[T-Nb_2O_5] (Supplementary Figs. 20 and 21). Entropy corrections at the finite temperature (300 K) originating from phonon contributions also stabilize the monoclinic phase by additional 0.58 meV per atom (for a total free-energy difference of 1.02 meV per atom) compared with the orthorhombic phase. For comparison, we also considered the stability of the monoclinic phase for the case of the pristine unlithiated [T-Nb_2O_5] unit cell (Fig. 3i) and found that in this case the orthorhombic phase is more stable. Therefore, the calculations predict that T-Nb_2O_5 will undergo a phase transition from orthorhombic to monoclinic at Li/Nb ≈ 0.5, in agreement with our experimental findings.

Electrochemical and electronic properties via Li intercalation

Epitaxial T-Nb_2O_5 single-crystalline thin films deposited on LSAT(110) substrates were characterized electrochemically in a typical Li-ion battery configuration allowing the quantification of inserted Li depending on the reaction speed. Li metal and carbonate-based electrolyte with $LiPF_6$ salt were used as anode/reference electrode and electrolyte, respectively (Methods and Supplementary Fig. 22). Galvanostatic cycling at current densities ranging from 1.43 to 14.3 A g^{-1} delivered the expected voltage versus capacity profile, with reversible capacities ranging from 130–80 mAh g^{-1} (Fig. 4a,b). This indicates another figure of merit representing the excellent intercalation kinetics for the epitaxial film in accord with previous reports on nanoparticles[34]. The electrochemical properties were also demonstrated by cyclic voltammetry for 16, 80 and 160 nm thick films (Fig. 4c and Supplementary Fig. 23).

To explore the electronic property changes of epitaxial T-Nb_2O_5 thin films upon lithiation, Hall devices for Li-ILG were fabricated with the Au/Ru gate electrode (Fig. 4d and Supplementary Fig. 24a). Before placing 0.3 M Li-TFSI in EMIM-TFSI (Li-ionic liquid (IL)) onto the device, we first measured temperature-dependent resistivity (RT) curves of pristine T-Nb_2O_5 films using a high resistance meter. The room temperature resistivity of the T-Nb_2O_5 film is 2.78×10^8 Ω cm (Supplementary Fig. 25), which is comparable with previous reports ranging from 10^7 to 10^9 Ω cm (refs. 43,44). After placing IL onto the device, the resistivity drops to ~5×10^{-1} Ω cm due to the lower resistance of the IL (~10^{14} Ω for T-Nb_2O_5 while ~10^6 Ω for IL when a source-drain current of 1 μA is applied; Supplementary Fig. 26). Therefore, before Li intercalation, the resistance of the device is determined by the resistance of the IL. We emphasize that the high limit of the resistivity accessible to the T-Nb_2O_5 material is given by the ex situ measured value, while at the low limit the resistivity is governed by the gated T-Nb_2O_5 film. The source-drain current- (I_{sd}) or voltage (V_{sd})-dependent resistance changes of IL alone show that the resistance of the IL decreases as increasing I_{sd}/V_{sd} (Supplementary Fig. 26), which is probably due to the leakage from IL decomposition at high voltages. Therefore, by adjusting the operating parameters of our device (for example, using a lower I_{sd}/V_{sd}), we can measure a larger resistivity change during gating. Note that, for simplicity of the resistivity calculations of the device, all resistivities were calculated using the film thickness and the channel dimensions of 65×30 μm^2. The RT curves at different gate voltages are shown in Fig. 4f. Notably, the resistivity after metallization is ~2×10^{-3} Ω cm, which is approximately 11 orders of magnitude smaller than that of pristine T-Nb_2O_5. Such a colossal insulator–metal transition is remarkable compared to the previously reported metallization by ILG[1–13] (Supplementary Fig. 28 and Supplementary Table 3).

https://doi.org/10.1038/s41563-023-01612-2

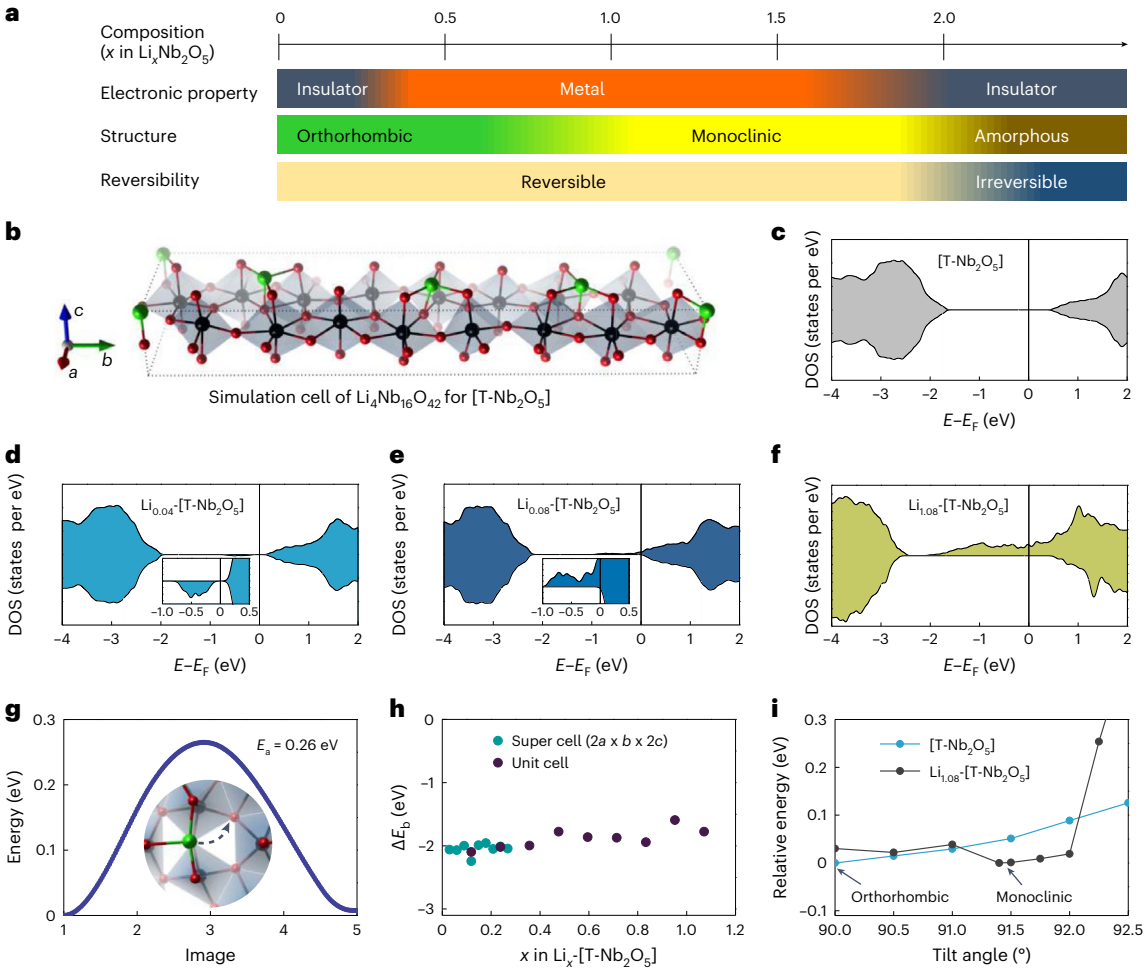

Fig. 3 | Electronic and structural phases of *T*-Nb_2O_5 via Li intercalation. **a**, Electronic and structural phase diagram of *T*-Nb_2O_5 film versus Li intercalation. The phase transitions and their reversibility are presented schematically. **b**, Structural model of the orthorhombic model system ($Li_4Nb_{16}O_{42}$), which was employed to simulate the conventional (pristine) unit cell of *T*-Nb_2O_5 ($Nb_{16.8}O_{42}$, shown in Supplementary Fig. 16), in which 4 Li are added per unit cell to replace the charge of the fractionally distributed 0.8 Nb atom/cell within the 4*g* layer. This model for *T*-Nb_2O_5 characterized by a $Li_4Nb_{16}O_{42}$ stoichiometry is considered as unlithiated and referred to as [*T*-Nb_2O_5] throughout. **c**, Total density of states (DOS) of the [*T*-Nb_2O_5] model unit cell. **d**,**e**, Total DOS with one and two extra Li intercalated into the ($a \times b \times 3c$) supercell of our simulation model (that is, $Li_{0.04}$-[*T*-Nb_2O_5] (**d**) and $Li_{0.08}$-[*T*-Nb_2O_5]) (**e**). **f**, Total DOS of the monoclinic $Li_{1.08}$-[*T*-Nb_2O_5] structure. **g**, Diffusion performance of the one extra Li in the primitive $Li_{0.12}$-[*T*-Nb_2O_5] unit cell, including free-energy profile and diffusion barrier (E_a). **h**, Evolution of the differential binding energy (ΔE_b) for low Li concentration within the supercell ($2a \times b \times 2c$) and at high concentration of Li within the primitive [*T*-Nb_2O_5] unit cell. **i**, The relative energy evolution of two lithiation states ([*T*-Nb_2O_5] and $Li_{1.08}$-[*T*-Nb_2O_5]) as a function of the monoclinic angle in the range between 90° and 92.5°.

To investigate the origin of metallization, the devices were gated between $V_g = 3$ and −2 V using conventional ILs, including DEME-TFSI, EMIM-TFSI and 0.3 M Li-TFSI in EMIM-TFSI (Li-IL) (Fig. 2g). While Li-ILG induces metallization, no noticeable change in resistivity was observed for pure IL. This contrasts with ILG of other oxide films, such as VO_2, WO_3 and $SrCoO_{2.5}$, all of which show metallization in the absence of Li ions due to oxygen or hydrogen ion migration[2–10]. The effect of the substrate orientation and film thickness on ILG is summarized in Supplementary Fig. 29. All films grown on (001)- and (110)-oriented substrates show good metallization behaviour owing to vertical ionic transport channels. For thicknesses ranging from 16 to 160 nm and gating with sufficiently slow voltage sweep rates, the resistivity at $V_g = 3$ V is close to 10^{-3} Ω cm, demonstrating that the metallization happens in the bulk of the material. This is further confirmed by hard X-ray absorption near-edge structure (XANES) measurements (Supplementary Fig. 30), where Nb K-absorption edge shifts to lower energy upon gating to positive potentials. This indicates the reduction of the Nb oxidation state in the bulk of the film, in agreement with prior work on a polycrystalline sample[45]. When we performed high voltage gating (Supplementary Figs. 31 and 32), the resistivity increased as the gating voltage was increased above 4.5 V, indicating the onset of a metal-to-insulator transition. The voltage-dependent carrier concentration, mobility and resistivity changes are summarized in Fig. 4h. The electronic transitions correlate well with the in situ X-ray diffraction data in Fig. 2a,f.

Tunable and low voltage operation by chemical potential control

The working voltage of a Li-ion battery cell depends on the difference in chemical potential between the cathode and the anode[18]. To exploit this, the Au gate electrode was replaced by conventional Li-containing electrode materials, namely $LiFePO_4$ (LFP), $LiCoO_2$ (LCO) and $Li_xNb_2O_5$ (LNbO). The Li intercalation potentials in these materials are ~3.5, 4.0 and 1.8 V versus Li^+/Li for LFP, LCO and LNbO, respectively, and are all within the electrochemical stability range of the IL used in this study. The fabrication process is described in Supplementary Section 6 and Fig. 4e, and the V_g-dependent resistivity (RV) curves with different

https://doi.org/10.1038/s41563-023-01612-2

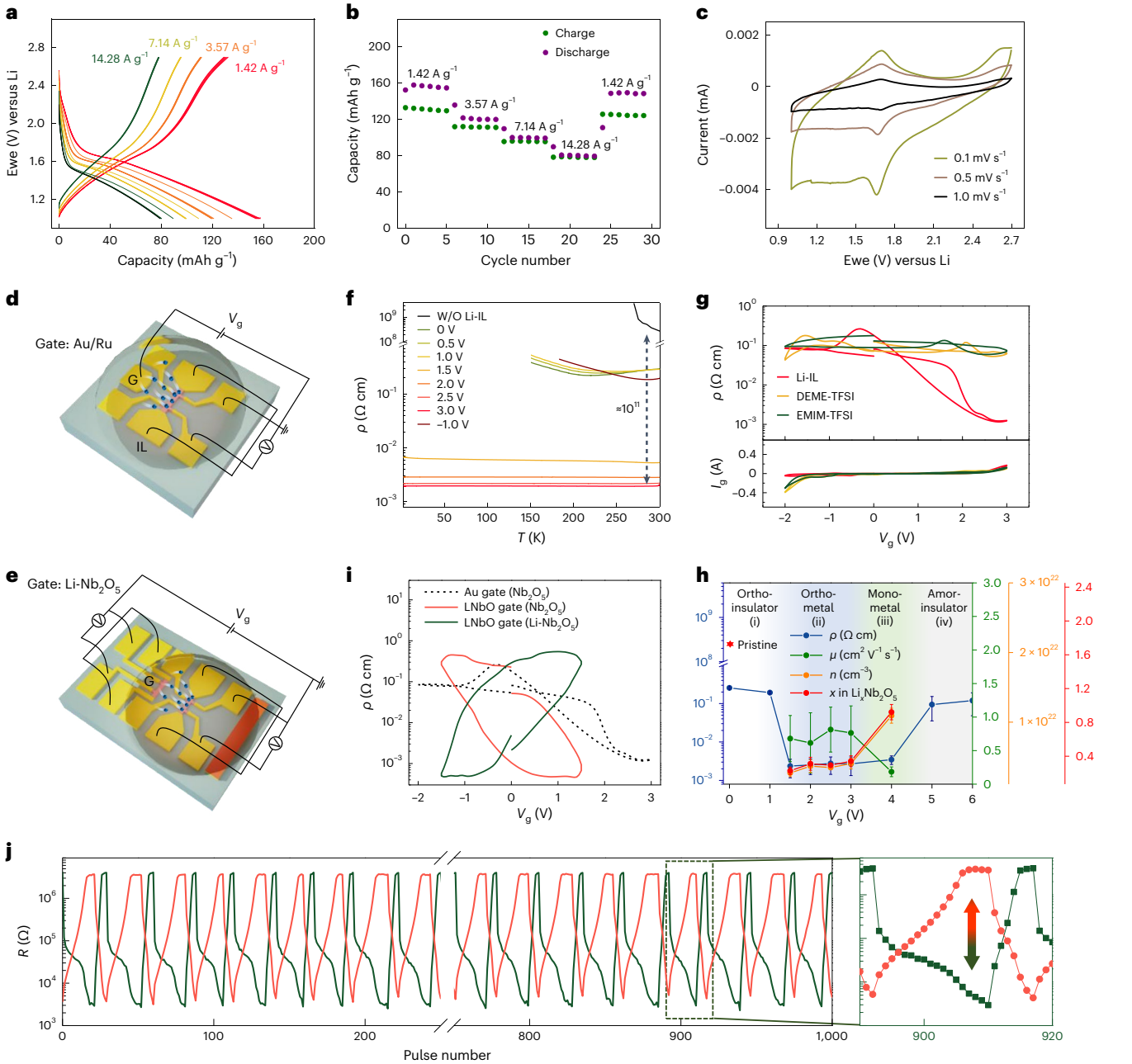

Fig. 4 | Electrochemical and electronic properties of epitaxial *T*-Nb_2O_5 thin films. a,**b**, Galvanostatic discharge–charge curves (**a**) and specific capacity obtained at each cycle (**b**) at different current rates for a 40 nm *T*-Nb_2O_5/LSAT(110). An irreversible capacity is observed at the slowest current densities, which is attributed to corrosion of parts of the device. **c**, Cyclic voltammogram recorded at different scan rates. The second cycle of each cycling rate is shown. **d**,**e**, Schematics of the ILG device with the Au gate electrode (**d**) and using the LNbO gate electrode (**e**). G represents gate electrode. Blue spheres denote Li-ion migrations from gating. **f**, Temperature-dependent resistivity curves at different gate voltages. **g**, V_g-dependent resistivity and leakage current curves for several ILs. The sweeping rate was 16 mV s^{-1}. **h**, V_g-dependent carrier concentration (n), Li composition (x), mobility (μ) and resistivity (ρ) curves from Hall measurements at 200 K for $Li_xNb_2O_5$. The mean and standard deviation are represented with the error bars after three measurements. The resistivity of the pristine film is indicated by the red pentacle. Multistep transitions are shown with increasing V_g, that is, (i) orthorhombic insulator (white regime), (ii) orthorhombic metal (blue), (iii) monoclinic metal (red) and (iv) insulating state (grey). The carrier concentration suddenly increases, and the mobility starts to decrease at ~4 V, indicating carrier scattering at high Li concentrations. The Li concentrations are obtained from Hall measurements, assuming that each Li atom creates one charge carrier. **i**, V_g-dependent ρ curves for the 16 nm *T*-Nb_2O_5/LSAT(110) devices using the LNbO gate electrode (blue and light blue curves) and the Au electrode (the dotted black curve). The sweeping rate was 16 mV s^{-1}. **j**, Pulse voltage gating of twin *T*-Nb_2O_5 devices. The device structure is depicted in **e**. Pulse voltages of 3 V/−3 V were applied with a pulse with of 50 ms. The channel resistances were measured at 1 μA (I_{sd}). The film thickness and channel size were 30 nm and 60 × 30 μm^2, respectively.

gate electrodes are shown in Supplementary Fig. 35. The critical metallization voltage (V_c) is defined from the peak of the normalized dρ/dV curves. The chemical potential (V versus Li/Li$^+$)-dependent V_c plot (Supplementary Fig. 35c) shows that V_c tends to decrease as the potential difference between the gate electrode and *T*-Nb_2O_5 decreases. Notably, the LNbO gate electrode leads to coupled resistivity changes between the LNbO gate electrode and Nb_2O_5 channel due to the ion exchange between them, and it reveals a substantial decrease in the V_c value of

~0.54 V compared to the Au electrode (Fig. 4i), which has been extensively used in typical ILG devices[2–5]. In particular, such potential control of V_c is not possible with conventional ILG based on proton insertion or oxygen ion loss, because the V_c will be determined by the more poorly determined electrochemical process that occurs at the counter (gate) electrode (including double layer formation, electrolyte degradation and oxygen evolution).

Pulsed voltage gating of *T*-Nb_2O_5 and WO_3 thin-film devices

We performed pulsed voltage gating on *T*-Nb_2O_5 and WO_3 thin-film devices to compare the kinetics of Li insertion and metallization (Supplementary Section 7). To explore the effects of the crystal orientation and the presence of crystallinity, devices were fabricated using an Au gate electrode, as depicted in Fig. 4d, for a 30 nm polycrystalline *T*-Nb_2O_5 thin film grown on a YSZ(001) substrate (Supplementary Fig. 36) and compared to the single-crystalline thin films deposited on LSAT(110) having the same thickness (Supplementary Fig. 39). The single-crystalline *T*-Nb_2O_5 device shows metallization after a single pulse of 4.3 V with a pulse width (*W*) of 0.8 s (Supplementary Fig. 39) while the polycrystalline *T*-Nb_2O_5 becomes metallic after 45 pulses, indicating that the vertical orientation of ionic channels plays a crucial role for the fast ionic gating. The critical resistivity for metallization was defined as 2×10^{-3} Ω cm, which shows a decrease in resistivity with decreasing temperature (Fig. 4f and Supplementary Fig. 38b). The pulse voltage (*H*)-dependent resistance changes of the single-crystalline *T*-Nb_2O_5 device are shown in Supplementary Fig. 37. Moreover, a 30 nm epitaxial WO_3 film (Supplementary Fig. 38) was gated with Li-IL at 3.5 V and pure IL (DEME-TFSI) at 4.3 V and shows metallization after 8 and ~1,500 pulses, respectively, showing that Li^+ ion gating is much faster than the O^{2-}/H^+ ion gating (Supplementary Fig. 39). Note that pulsed voltage gating above 4 V on WO_3 with Li-IL leads to increased resistance compared to 3.5 V (Supplementary Fig. 38c), which is probably due to a conversion reaction[31], limiting higher voltage operation. Single-crystalline *T*-Nb_2O_5 features a resistance change by ~11 orders from the initially insulating film to the gated metallic film by a single pulse, while for WO_3 the change is ~6 orders of magnitude (Supplementary Fig. 39b). The pulsed width-dependent resistance changes (Supplementary Fig. 40) further reveal the larger resistance changes of the single-crystalline *T*-Nb_2O_5 thin film compared to the WO_3 thin film in the electrochemical reaction region.

The single-crystalline *T*-Nb_2O_5 device with an Au gate electrode reveals one order of magnitude resistance change over ~3.5×10^5 pulses (3.8 V/−2 V with a pulse width of 50 ms), illustrating good reversibility (Supplementary Fig. 41). In particular, by replacing the Au gate electrode with Li-Nb_2O_5 (Fig. 4e), coupled responses between twin *T*-Nb_2O_5 devices are realized (Fig. 4j). The resistances of the two devices oscillate out of phase for three orders of magnitude for more than 10^3 pulses, when applying 3 V/−3 V and a pulse width of 50 ms.

In summary, we have realized the growth of single-crystalline epitaxial *T*-Nb_2O_5 thin films with vertically oriented 2D channels that provide paths for fast ionic migration. This morphology allows us to study the evolution of the electronic and structural properties during Li-ILG by comprehensive in situ and ex situ experiments. They reveal unexplored sequential phase transformations, including an orthorhombic insulator, an orthorhombic metal, a monoclinic metal and a degraded insulating phase, as Li concentration is increased. DFT calculations further support that the monoclinic phase (approximately $Li_1Nb_2O_5$) is energetically favourable and metallic. Defect electronic states near the Fermi energy from Li-ion migration lead to abrupt changes in resistivity. Thus, the *T*-Nb_2O_5 films with vertical ionic transport channels undergo substantial electrical change in an early stage of Li insertion into the initially insulating d^0 films, leading to a colossal insulator–metal transition with a change in resistance of 11 orders of magnitude. The *T*-Nb_2O_5 film shows an even larger and faster resistance change and a wider voltage operation range via Li interaction, compared with WO_3 thin films, which are one of the best electrochemical materials. Moreover, coupled electronic responses between twin *T*-Nb_2O_5 devices are demonstrated through ionic exchange between each other. This work showcases a synergistic experiment–theory approach to develop new ionically channelled devices for diverse applications, including thin-film batteries, electrochromic devices, neuromorphic devices and electrochemical random-access memory.

Online content

Any methods, additional references, Nature Portfolio reporting summaries, source data, extended data, supplementary information, acknowledgements, peer review information; details of author contributions and competing interests; and statements of data and code availability are available at https://doi.org/10.1038/s41563-023-01612-2.

References

1. Guan, Y., Han, H., Li, F., Li, G. & Parkin, S. S. P. Ionic gating for tuning electronic and magnetic properties. *Ann. Rev. Mater. Res.* **53**, 25–51 (2023).
2. Jeong, J. et al. Suppression of metal-insulator transition in VO_2 by electric field-induced oxygen vacancy formation. *Science* **339**, 1402–1405 (2013).
3. Jeong, J. et al. Giant reversible, facet-dependent, structural changes in a correlated-electron insulator induced by ionic liquid gating. *Proc. Natl Acad. Sci. USA* **112**, 1013–1018 (2015).
4. Lu, N. et al. Electric-field control of tri-state phase transformation with a selective dual-ion switch. *Nature* **546**, 124–128 (2017).
5. Leng, X. et al. Insulator to metal transition in WO_3 induced by electrolyte gating. *npj Quant. Mater.* **2**, 35 (2017).
6. Hope, M. A. et al. The role of ionic liquid breakdown in the electrochemical metallization of VO_2: an NMR study of gating mechanisms and VO_2 reduction. *J. Am. Chem. Soc.* **140**, 16685–16696 (2018).
7. Han, H. et al. Control of oxygen vacancy ordering in brownmillerite thin films via ionic liquid gating. *ACS Nano* **16**, 6206–6214 (2022).
8. Han, H. et al. Strain-driven formation of epitaxial nanostructures in brownmillerite strontium cobaltite thin films. *Proc. Natl Acad. Sci. USA* **120**, e2221651120 (2023).
9. Altendorf, S. G. et al. Facet-independent electric-field-induced volume metallization of tungsten trioxide films. *Adv. Mater.* **28**, 5284–5292 (2016).
10. Wang, M. et al. Electric-field-controlled phase transformation in WO_3 thin films through hydrogen evolution. *Adv. Mater.* **29**, 1703628 (2017).
11. Perez-Muñoz, A. M. et al. In-situ evidence of deoxygenation in ionic liquid gating of $YBa_2Cu_3O_{7-x}$. *Proc. Natl Acad. Sci. USA* **114**, 215–220 (2017).
12. Passarello, D. et al. Evidence for ionic liquid gate-induced metallization of vanadium dioxide bars over micron length scales. *Nano Lett.* **17**, 2796–2801 (2017).
13. Cui, B. et al. Direct imaging of structural changes induced by ionic liquid gating leading to engineered three-dimensional meso-structures. *Nat. Commun.* **9**, 3055 (2018).
14. Tarascon, J. M. & Armand, M. Issues and challenges facing rechargeable lithium batteries. *Nature* **414**, 359–367 (2001).
15. Xu, K. Electrolytes and interphases in Li-ion batteries and beyond. *Chem. Rev.* **114**, 11503–11618 (2014).
16. Griffith, K. J., Wiaderek, K. M., Cibin, G., Marbella, L. E. & Grey, C. P. Niobium tungsten oxides for high-rate lithium-ion energy storage. *Nature* **559**, 556–563 (2018).
17. Kang, B. & Ceder, G. Battery materials for ultrafast charging and discharging. *Nature* **458**, 190–193 (2009).

18. Liu, C., Neale, Z. G. & Cao, G. Understanding electrochemical potentials of cathode materials in rechargeable batteries. *Mater. Today* **19**, 109–123 (2016).
19. Sood, A. et al. Electrochemical ion insertion from the atomic to the device scale. *Nat. Rev. Mater.* **6**, 847–867 (2021).
20. Dahlman, C. J. et al. Dynamics of lithium insertion in electrochromic titanium dioxide nanocrystal ensembles. *J. Am. Chem. Soc.* **143**, 8278–8294 (2021).
21. Lu, H. C. et al. Synthesis and dual-mode electrochromism of anisotropic monoclinic $Nb_{12}O_{29}$ colloidal nanoplatelets. *ACS Nano* **14**, 10068–10082 (2020).
22. Granqvist, C. G. Electrochromic oxides: a bandstructure approach. *Sol. Energy Mater. Sol. Cells* **32**, 369–382 (1994).
23. Li, Y. et al. Low-voltage, CMOS-free synaptic memory based on Li_xTiO_2 redox transistors. *ACS Appl. Mater. Interfaces* **11**, 38982–38992 (2019).
24. Fuller, E. J. et al. Li-ion synaptic transistor for low power analog computing. *Adv. Mater.* **29**, 1604310 (2017).
25. Zhu, Y. et al. Lithium-film ceramics for solid-state lithionic devices. *Nat. Rev. Mater.* **6**, 313–331 (2020).
26. Marianetti, C. A., Kotliar, G. & Ceder, G. A first-order Mott transition in Li_xCoO_2. *Nat. Mater.* **3**, 627–631 (2004).
27. Sun, Y. et al. Strongly correlated perovskite lithium ion shuttles. *Proc. Natl Acad. Sci. USA* **115**, 9672–9677 (2018).
28. Griffith, K. J. et al. Ionic and electronic conduction in $TiNb_2O_7$. *J. Am. Chem. Soc.* **141**, 16706–16725 (2019).
29. Tang, J. et al. ECRAM as scalable synaptic cell for high-speed, low-power neuromorphic computing. In *IEEE International Electron Devices Meeting* 13.1.1–13.1.4 (IEEE, 2018).
30. Muscher, P. K. et al. Highly efficient uniaxial in-plane stretching of a 2D material via ion insertion. *Adv. Mater.* **33**, 2101875 (2021).
31. He, Y. et al. Atomistic conversion reaction mechanism of WO_3 in secondary ion batteries of Li, Na, and Ca. *Angew. Chem. Int. Ed. Engl.* **55**, 6244–6247 (2016).
32. Griffith, K. J., Forse, A. C., Griffin, J. M. & Grey, C. P. High-rate intercalation without nanostructuring in metastable Nb_2O_5 bronze phases. *J. Am. Chem. Soc.* **138**, 8888–8899 (2016).
33. Chen, D. et al. Unraveling the nature of anomalously fast energy storage in T-Nb_2O_5. *J. Am. Chem. Soc.* **139**, 7071–7081 (2017).
34. Augustyn, V. et al. High-rate electrochemical energy storage through Li^+ intercalation pseudocapacitance. *Nat. Mater.* **12**, 518–522 (2013).
35. Kim, J. W., Augustyn, V. & Dunn, B. The effect of crystallinity on the rapid pseudocapacitive response of Nb_2O_5. *Adv. Energy Mater.* **2**, 141–148 (2012).
36. Lübke, M. et al. High power nano-Nb_2O_5 negative electrodes for lithium-ion batteries. *Electrochim. Acta* **192**, 363–369 (2016).
37. Brauer, G. Die Oxyde des Niobs. *Z. Anorg. Allg. Chem.* **248**, 1–31 (1941).
38. Nico, C., Monteiro, T. & Graça, M. P. F. Niobium oxides and niobates physical properties: review and prospects. *Prog. Mater. Sci.* **80**, 1–37 (2016).
39. Kato, K. & Tamura, S. Die Kristallstruktur von *T*-Nb_2O_5. *Acta Cryst.* **B31**, 673 (1975).
40. Boschker, J. E., Markurt, T., Albrecht, M. & Schwarzkopf, J. Heteroepitaxial growth of T-Nb_2O_5 on $SrTiO_3$. *Nanomaterials* **8**, 895 (2018).
41. Seo, J. W., Dieker, C., Fompeyrine, J., Siegwart, H. & Locquet, J.-P. Structural domains in antiferromagnetic $LaFeO_3$ thin films. *Int. J. Mater. Res.* **97**, 943–947 (2006).
42. Leriche, J.B. et al. An electrochemical cell for operando study of lithium batteries using synchrotron radiation. *J. Electrochem. Soc.* **157**, A606–A610 (2010).
43. Barnes, P. et al. Electrochemically induced amorphous-to-rock-salt phase transformation in niobium oxide electrode for Li-ion batteries. *Nat. Mater.* **21**, 795–803 (2022).
44. Kowalski, D., Aoki, Y. & Habazaki, H. Characterization of amorphous anodic Nb_2O_5 nanofilm for gas sensing. *ECS Trans.* **16**, 57–65 (2009).
45. Kodama, R., Terada, Y., Nakai, I., Komaba, S. & Kumagai, N. Electrochemical and in situ XAFS-XRD investigation of Nb_2O_5 for rechargeable lithium batteries. *J. Electrochem. Soc.* **153**, A583–A588 (2006).

Methods

Film growth

A RHEED-assisted PLD system using a 248 nm KrF excimer laser was employed to optimize the growth conditions of Nb_2O_5 thin films by varying the growth temperature from 500 to 900 °C. The laser fluence, oxygen partial pressure (pO_2) and repetition rate were 1 J cm^{-2}, 10 mT and 6 Hz, respectively. The optimized growth temperature of T-Nb_2O_5 thin films was ~620 °C. The heating and cooling rates were 30 and 10 °C min^{-1}, respectively. Substrates of LSAT(001), LAO(001), LSAT(110) and LAO(110) were used to study substrate orientation-dependent domain structures. A YSZ(001) substrate was used to grow a polycrystalline T-Nb_2O_5 thin film. For gate electrode potential control, LFP and LCO thin films were grown on LSAT(110) substrates by varying pO_2 at room temperature. The laser fluence and repetition rate were 1 J cm^{-2} and 6 Hz, respectively. The optimal pO_2 was 1 mT and 10 mT for the LFP and LCO thin films, respectively, as determined by X-ray photoelectron spectroscopy (XPS) characterization. A WO_3 thin film was grown on a LAO(001) substrate. The growth temperature, laser fluence, oxygen partial pressure (pO_2) and repetition rate were 600 °C, 1 J cm^{-2}, 200 mT and 6 Hz, respectively. The film thickness was characterized by X-ray reflectivity measurements or fringes of theta–2theta scans, and the T-Nb_2O_5 thickness was further confirmed by TEM measurements.

Ionic liquid gating device fabrication

Standard photolithographic techniques were used to fabricate ionic liquid gating devices. Substrates with a size of 5 × 5 mm^2 were used. A T-Nb_2O_5 channel with a size of 65 × 30 μm^2 was etched and then Ru (5 nm) and Au (70 nm) layers were successively deposited using ion beam sputtering (SCIA coat 200) for both the gate electrode and channel contacts. The IL covered both the T-Nb_2O_5 and the gate electrode. For the gate electrode potential control, Li ion-containing oxides were deposited on top of the Au/Ru gate electrode.

For the LNbO gate electrode device fabrication, both channel and gate were etched, and then Au (70 nm)/Ru (5 nm) layers were deposited to make channel and gate contacts. Then, the reference electrode (LFP) was deposited using pulsed laser deposition. After the device fabrication, Li ions were moved from the LFP to the gate electrode by ILG to make the LNbO gate electrode. Then, the gating was applied to the Nb_2O_5 channel using the LNbO gate electrode.

For the in situ X-ray diffraction measurements of the thin films, a T-Nb_2O_5 channel with a dimension of 2 × 2 mm^2 was etched, then Au (70 nm)/Ru(5 nm) layers were deposited for the gate electrode and channel contacts. The device was then attached using double-sided tape to a specially designed sample holder. The IL was placed on the device surface, and then Kapton film was attached to reduce the thickness of the IL. Resistance and θ–2θ scans were measured during in situ ILG.

Thin-film characterization

The θ–2θ scans, phi scans and in situ X-ray diffraction on the thin films were carried out using a Bruker D8 Discovery X-ray diffractometer with CuKα radiation. Reciprocal space map measurements were performed using a Ga jet X-ray source (λ = 1.34 Å) and a six-circle diffractometer equipped with a Pilatus 100 K pixel detector. HAADF-STEM imaging was performed using a JEOL ARM200F with a spherical aberration corrector (CEOS) operated at 200 kV. XPS (K-Alpha, Thermo Scientific) was conducted for Li ion-containing oxides. The film surface was gently cleaned by cluster ion etching before the measurement.

Diethylmethyl(2-methoxyethyl)ammonium bis(trifluoromethylsulfonyl)imide (DEME-TFSI), 1-ethyl-3-methylimidazolium bis(trifluoromethylsulfonyl)imide (EMIM-TFSI) and Li-IL were used for the ILG. For the Li-IL, a lithium bis(trifluoromethanesulfonyl)imide (Li-TFSI) powder was dissolved in the EMIM-IL at 50 °C for 2 h to achieve a solution of molality 0.3 mol kg^{-1}. Each IL was dried in a vacuum chamber (10^{-6} mbar) at 105 °C for at least 10 h before use.

Transport measurements of the ILG devices were carried out in a physical property measurement system (Quantum Design). Gate voltages were applied using a Keithley 2450A source meter. For the resistance measurements, a constant current of 1 μA was applied using a Keithley 6221 current source, and the voltage was measured by a Keithley 2182A nano-voltmeter. The gate voltage was applied between the gate electrode and the T-Nb_2O_5 channel while monitoring the resistance of the channel. The substrate is insulating, thus the voltage was applied through the IL, resulting in Li-ion migration from gating. The resistance of the pristine T-Nb_2O_5 and WO_3 thin films was measured by a high resistance meter (B2985A, KEYSIGHT). A total of 1,000 data points were averaged at each temperature in a probe station. Li-ILG of thin films for the ex situ X-ray diffraction, STEM and X-ray absorption near-edge structure measurements were carried out using a polytetrafluoroethylene boat with an Au plate (the gate electrode) covered with the Li-IL.

The pulsed voltage gating was performed in a probe station (CRX; Lake Shore). Gate voltages were applied using a Keithley 2636B source meter. A constant current of 1 μA was applied using a Keithley 6221 current source, and the voltage was measured by a Keithley 2182A nano-voltmeter to measure the channel resistance. The 6221/2182A system is advantageous for the fast readouts after the pulsed gating and provides electrical floating between each device.

The Nb K-edge X-ray absorption spectra were acquired at the CLÆSS beamline at the ALBA synchrotron[46]. The synchrotron radiation emitted by a wiggler source was monochromatized using a double crystal Si(311) monochromator, while higher harmonics were rejected by proper choice of angles and coatings of the collimating and focusing mirrors. The samples were mounted in a liquid nitrogen cryostat, and the spectra were recorded in fluorescence mode at 80 K by means of a multichannel silicon drift detector. The sample normal and the fluorescence detector were at 60 and 90 degrees with respect to the incoming beam, respectively. The fluorescence detector dead time was kept around 4.5% at 19,600 eV for both samples for a better comparison.

Powder X-ray diffraction

Free-standing electrodes for in situ X-ray diffraction measurements with coupled electrochemistry were prepared by mixing 90 wt% T-Nb_2O_5 powder (Sigma-Aldrich), 5 wt.% polytetrafluoroethylene binder, 5 wt% carbon black (Timcal SuperP). The mixed powder was pressed and rolled onto a flat surface to give a homogeneous film. The film was formed into a disc with a diameter of 13 mm and dried in a Büchi oven at 100 °C under dynamic vacuum (10^{-2} mbar) for 12 h before transferring into an argon-filled glovebox. A customized electrochemical cell equipped with a Be window was used to prepare cells for in situ X-ray diffraction. The 70 μl of LP57 electrolyte (1 M $LiPF_6$, ethylene carbonate/ethyl methyl carbonate (3/7), SoulBrain) was added to the film followed by 16 mm glass fibre separator. Battery cycling was conducted using a Land cycler at room temperature between open circuit voltage and 0.005 V at C/34 rate (34 hours for a full charge–discharge). In situ X-ray diffraction data were collected at 300 K on a Panalytical Empyrean diffractometer equipped with a Ni filter using CuKα radiation (λ = 1.5406 Å) in Bragg–Bentano geometry. Ex situ SXRD measurement were performed in Kapton capillaries at 11-BM beamline of the Advanced Photon Source (APS). Lithiated $Li_{1.2}Nb_2O_5$ and $Li_{1.6}Nb_2O_5$ powders were prepared in a swagelok type cell using LP57, glass fiber and Li metal as electrolyte, separator and counter electrode, respectively. In situ SXRD was performed in half cell configuration using the Ampix operando cell at the APS.

Electrochemical characterization

For electrochemical cycling of thin films in a pouch cell, the samples were deposited on non-conducting LSAT substrates giving highly oriented single-crystalline films. For the current collector, Au was deposited/patterned on the surface of the thin film. The Cu tab was

connected on the gold pattern (Supplementary Fig. 7). The other components of cell, anode, electrolyte and separator were the same as those used for the in situ powder X-ray diffraction experiments. The C rate was defined on the basis of 201.7 mAh g^{-1}, that is, one electron reduction per Nb_2O_5. For cyclic voltammetry experiments, three different scan rates of 0.1, 0.5 and 1.0 mV s^{-1} were used. Galvanostatic charge–discharge was also performed with current densities of 14.28, 7.14, 3.57 and 1.43 A g^{-1}. The thin-film capacity was determined from the dimensions (surface × thickness) and the specific capacity of T-Nb_2O_5 (175 mAh g^{-1}). The film thickness was determined by X-ray reflectivity measurements (Supplementary Fig. 2b) and further confirmed by TEM measurements. The electroactive surface was considered to be delimited by the Au pattern (0.12 mm^2).

DFT calculations

The unit cell of unlithiated [T-Nb_2O_5] ($Li_4Nb_{16}O_{42}$ in our model) is described in Supplementary Section 3.2. We modelled the diffusion of one Li ion in the unit cell of T-Nb_2O_5 by the nudged elastic band method with climbing image (CI-NEB). The free-energy profile of the most favourable diffusion pathway has been shown in Fig. 3g.

The differential binding energy (ΔE_b) of each Li interstitial reaction in the [T-Nb_2O_5] model (as shown in Fig. 3h) was calculated as:

$$\Delta E_b = E(Li_{x'}\text{-}[T\text{-}Nb_2O_5]) - E(Li_{x'}\text{-}[T\text{-}Nb_2O_5]) - 0.5(x - x') \times n_{Nb}E(Li)\ (n_{Nb} = 16.8 \text{ or } 67.2)$$

where n_{Nb} indicates the number of Nb atoms in the cell, and $0.5(x - x') \times n_{Nb}$ is the number of extra Li atoms intercalated into the material. E indicates the DFT energies of the compositions calculated from ab initio studies. The reference energy of E(Li) is calculated from bulk Li metal. The energy of [T-Nb_2O_5] is calculated from our unit cell model of $Li_4Nb_{16}O_{42}$ and supercell of $Li_{16}Nb_{64}O_{168}$, respectively. All possible interstitial sites for each Li atom were considered and the site providing the most negative ΔE_b is the most energetically favourable location for that atom (these sites are shown in Supplementary Fig. 20). Such an arrangement of interstitial Li was used iteratively as a starting configuration for the higher concentration simulations. More detailed computational methods are shown in Supplementary Section 3.1.

Reporting summary

Further information on research design is available in the Nature Portfolio Reporting Summary linked to this article.

Data availability

The main data that support the results of this study are available within this Article and its Supplementary Information.

Reference

46. Simonelli, L. et al. CLÆSS: the hard X-ray absorption beamline of the ALBA CELLS synchrotron. *Cogent Phys.* **3**, 1231987 (2016).

Acknowledgements

This project has received funding from the European Union's Horizon 2020 research and innovation programme under grant agreement no. 737109. Funding has been provided by the Alexander von Humboldt Foundation in the framework of the Alexander von Humboldt Professorship to S.S.P.P. endowed by the Federal Ministry of Education and Research. The electrochemical theory of Z.J. and A.K. was supported by the US Department of Energy, Office of Science, Basic Energy Sciences, under award no. DE-SC0019281. F.N.S. acknowledges funding from the Faraday Institution CATMAT project (FIRG016). The oxide structure and phase transition theory of A.M.S. and A.M.R. was supported by the Office of Naval Research, under grant N00014-20-1-2701. The authors acknowledge computational support from the National Energy Research Scientific Computing Center (NERSC) of the DOE and the High-Performance Computing Modernization Office (HPCMO) of the US Department of Defense (DOD). Use of the APS at Argonne National Laboratory was supported by the US Department of Energy, Office of Science, Office of Basic Energy Sciences, under contract No. DE-AC02-06CH11357. We thank C. Guillemard at ALBA synchrotron and J. H. Jin at GERI for their assistance with gating of XANES and TEM samples, respectively.

Author contributions

H.H., Q.J., C.P.G. and S.S.P.P. conceived the project. H.H. grew and characterized thin films. H.H. and A.S. fabricated ILG devices. H.H. performed transport measurements. H.H. and J.-C.J. carried out the pulsed voltage gating and high resistance measurements. Q.J. and F.N.S. contributed to electrochemical measurements. Q.J., F.N.S. and K.J.G. analysed powder structures. H.H. and H.L.M. analysed thin-film structures. S.Y.N. and J.P. performed TEM. L.S. carried out XANES. Z.J., A.M.S. and A.K. performed DFT calculations. H.H. was the lead researcher. C.P.G., A.M.R. and S.S.P.P. supervised the project. H.H., Q.J., Z.J., C.P.G., A.M.R. and S.S.P.P. wrote the manuscript with contributions from all authors.

Funding

Open access funding provided by Max Planck Society.

Competing interests

The authors declare no competing interests.

Additional information

Supplementary information The online version contains supplementary material available at https://doi.org/10.1038/s41563-023-01612-2.

Correspondence and requests for materials should be addressed to Hyeon Han, Andrew M. Rappe, Clare P. Grey or Stuart S. P. Parkin.

Peer review information *Nature Materials* thanks the anonymous reviewers for their contribution to the peer review of this work.

nature portfolio

Corresponding author(s): Hyeon Han, Andrew M. Rappe, Clare P. Grey, Stuart S. P. Parkin

Last updated by author(s): Jun 18, 2023

Reporting Summary

Nature Portfolio wishes to improve the reproducibility of the work that we publish. This form provides structure for consistency and transparency in reporting. For further information on Nature Portfolio policies, see our Editorial Policies and the Editorial Policy Checklist.

Statistics

For all statistical analyses, confirm that the following items are present in the figure legend, table legend, main text, or Methods section.

n/a	Confirmed	
☐	☒	The exact sample size (*n*) for each experimental group/condition, given as a discrete number and unit of measurement
☐	☒	A statement on whether measurements were taken from distinct samples or whether the same sample was measured repeatedly
☒	☐	The statistical test(s) used AND whether they are one- or two-sided *Only common tests should be described solely by name; describe more complex techniques in the Methods section.*
☒	☐	A description of all covariates tested
☐	☒	A description of any assumptions or corrections, such as tests of normality and adjustment for multiple comparisons
☐	☒	A full description of the statistical parameters including central tendency (e.g. means) or other basic estimates (e.g. regression coefficient) AND variation (e.g. standard deviation) or associated estimates of uncertainty (e.g. confidence intervals)
☒	☐	For null hypothesis testing, the test statistic (e.g. *F*, *t*, *r*) with confidence intervals, effect sizes, degrees of freedom and *P* value noted *Give P values as exact values whenever suitable.*
☒	☐	For Bayesian analysis, information on the choice of priors and Markov chain Monte Carlo settings
☒	☐	For hierarchical and complex designs, identification of the appropriate level for tests and full reporting of outcomes
☒	☐	Estimates of effect sizes (e.g. Cohen's *d*, Pearson's *r*), indicating how they were calculated

Our web collection on statistics for biologists contains articles on many of the points above.

Software and code

Policy information about availability of computer code

Data collection	Irrelevant to experiments.
Data analysis	The TEM images were analyzed by Gatan Microscopy Suite (GMS) (3.3). The first-principles calculation were performed using the QUANTUM ESPRESSO (QE) package.

For manuscripts utilizing custom algorithms or software that are central to the research but not yet described in published literature, software must be made available to editors and reviewers. We strongly encourage code deposition in a community repository (e.g. GitHub). See the Nature Portfolio guidelines for submitting code & software for further information.

Data

Policy information about availability of data

All manuscripts must include a data availability statement. This statement should provide the following information, where applicable:

- Accession codes, unique identifiers, or web links for publicly available datasets
- A description of any restrictions on data availability
- For clinical datasets or third party data, please ensure that the statement adheres to our policy

The main data that support the results of this study are available within this Article and Supplementary Information.

Human research participants

Policy information about studies involving human research participants and Sex and Gender in Research.

Reporting on sex and gender	*Use the terms sex (biological attribute) and gender (shaped by social and cultural circumstances) carefully in order to avoid confusing both terms. Indicate if findings apply to only one sex or gender; describe whether sex and gender were considered in study design whether sex and/or gender was determined based on self-reporting or assigned and methods used. Provide in the source data disaggregated sex and gender data where this information has been collected, and consent has been obtained for sharing of individual-level data; provide overall numbers in this Reporting Summary. Please state if this information has not been collected. Report sex- and gender-based analyses where performed, justify reasons for lack of sex- and gender-based analysis.*
Population characteristics	*Describe the covariate-relevant population characteristics of the human research participants (e.g. age, genotypic information, past and current diagnosis and treatment categories). If you filled out the behavioural & social sciences study design questions and have nothing to add here, write "See above."*
Recruitment	*Describe how participants were recruited. Outline any potential self-selection bias or other biases that may be present and how these are likely to impact results.*
Ethics oversight	*Identify the organization(s) that approved the study protocol.*

Note that full information on the approval of the study protocol must also be provided in the manuscript.

Field-specific reporting

Please select the one below that is the best fit for your research. If you are not sure, read the appropriate sections before making your selection.

☐ Life sciences ☐ Behavioural & social sciences ☐ Ecological, evolutionary & environmental sciences

For a reference copy of the document with all sections, see nature.com/documents/nr-reporting-summary-flat.pdf

Life sciences study design

All studies must disclose on these points even when the disclosure is negative.

Sample size	*Describe how sample size was determined, detailing any statistical methods used to predetermine sample size OR if no sample-size calculation was performed, describe how sample sizes were chosen and provide a rationale for why these sample sizes are sufficient.*
Data exclusions	*Describe any data exclusions. If no data were excluded from the analyses, state so OR if data were excluded, describe the exclusions and the rationale behind them, indicating whether exclusion criteria were pre-established.*
Replication	*Describe the measures taken to verify the reproducibility of the experimental findings. If all attempts at replication were successful, confirm this OR if there are any findings that were not replicated or cannot be reproduced, note this and describe why.*
Randomization	*Describe how samples/organisms/participants were allocated into experimental groups. If allocation was not random, describe how covariates were controlled OR if this is not relevant to your study, explain why.*
Blinding	*Describe whether the investigators were blinded to group allocation during data collection and/or analysis. If blinding was not possible, describe why OR explain why blinding was not relevant to your study.*

Behavioural & social sciences study design

All studies must disclose on these points even when the disclosure is negative.

Study description	*Briefly describe the study type including whether data are quantitative, qualitative, or mixed-methods (e.g. qualitative cross-sectional, quantitative experimental, mixed-methods case study).*
Research sample	*State the research sample (e.g. Harvard university undergraduates, villagers in rural India) and provide relevant demographic information (e.g. age, sex) and indicate whether the sample is representative. Provide a rationale for the study sample chosen. For studies involving existing datasets, please describe the dataset and source.*
Sampling strategy	*Describe the sampling procedure (e.g. random, snowball, stratified, convenience). Describe the statistical methods that were used to predetermine sample size OR if no sample-size calculation was performed, describe how sample sizes were chosen and provide a rationale for why these sample sizes are sufficient. For qualitative data, please indicate whether data saturation was considered, and what criteria were used to decide that no further sampling was needed.*

Data collection	*Provide details about the data collection procedure, including the instruments or devices used to record the data (e.g. pen and paper, computer, eye tracker, video or audio equipment) whether anyone was present besides the participant(s) and the researcher, and whether the researcher was blind to experimental condition and/or the study hypothesis during data collection.*
Timing	*Indicate the start and stop dates of data collection. If there is a gap between collection periods, state the dates for each sample cohort.*
Data exclusions	*If no data were excluded from the analyses, state so OR if data were excluded, provide the exact number of exclusions and the rationale behind them, indicating whether exclusion criteria were pre-established.*
Non-participation	*State how many participants dropped out/declined participation and the reason(s) given OR provide response rate OR state that no participants dropped out/declined participation.*
Randomization	*If participants were not allocated into experimental groups, state so OR describe how participants were allocated to groups, and if allocation was not random, describe how covariates were controlled.*

Ecological, evolutionary & environmental sciences study design

All studies must disclose on these points even when the disclosure is negative.

Study description	*Briefly describe the study. For quantitative data include treatment factors and interactions, design structure (e.g. factorial, nested, hierarchical), nature and number of experimental units and replicates.*
Research sample	*Describe the research sample (e.g. a group of tagged Passer domesticus, all Stenocereus thurberi within Organ Pipe Cactus National Monument), and provide a rationale for the sample choice. When relevant, describe the organism taxa, source, sex, age range and any manipulations. State what population the sample is meant to represent when applicable. For studies involving existing datasets, describe the data and its source.*
Sampling strategy	*Note the sampling procedure. Describe the statistical methods that were used to predetermine sample size OR if no sample-size calculation was performed, describe how sample sizes were chosen and provide a rationale for why these sample sizes are sufficient.*
Data collection	*Describe the data collection procedure, including who recorded the data and how.*
Timing and spatial scale	*Indicate the start and stop dates of data collection, noting the frequency and periodicity of sampling and providing a rationale for these choices. If there is a gap between collection periods, state the dates for each sample cohort. Specify the spatial scale from which the data are taken*
Data exclusions	*If no data were excluded from the analyses, state so OR if data were excluded, describe the exclusions and the rationale behind them, indicating whether exclusion criteria were pre-established.*
Reproducibility	*Describe the measures taken to verify the reproducibility of experimental findings. For each experiment, note whether any attempts to repeat the experiment failed OR state that all attempts to repeat the experiment were successful.*
Randomization	*Describe how samples/organisms/participants were allocated into groups. If allocation was not random, describe how covariates were controlled. If this is not relevant to your study, explain why.*
Blinding	*Describe the extent of blinding used during data acquisition and analysis. If blinding was not possible, describe why OR explain why blinding was not relevant to your study.*

Did the study involve field work? ☐ Yes ☐ No

Field work, collection and transport

Field conditions	*Describe the study conditions for field work, providing relevant parameters (e.g. temperature, rainfall).*
Location	*State the location of the sampling or experiment, providing relevant parameters (e.g. latitude and longitude, elevation, water depth).*
Access & import/export	*Describe the efforts you have made to access habitats and to collect and import/export your samples in a responsible manner and in compliance with local, national and international laws, noting any permits that were obtained (give the name of the issuing authority, the date of issue, and any identifying information).*
Disturbance	*Describe any disturbance caused by the study and how it was minimized.*

Reporting for specific materials, systems and methods

We require information from authors about some types of materials, experimental systems and methods used in many studies. Here, indicate whether each material, system or method listed is relevant to your study. If you are not sure if a list item applies to your research, read the appropriate section before selecting a response.

Materials & experimental systems

n/a	Involved in the study
☒	☐ Antibodies
☒	☐ Eukaryotic cell lines
☒	☐ Palaeontology and archaeology
☒	☐ Animals and other organisms
☒	☐ Clinical data
☒	☐ Dual use research of concern

Methods

n/a	Involved in the study
☒	☐ ChIP-seq
☒	☐ Flow cytometry
☒	☐ MRI-based neuroimaging